A Hybrid Control Strategy of LCC–LCC Compensated Electric Vehicles Wireless Charging System With Wide ZVS Range

Jinlin Peng, Bo Zhang, *Fellow, IEEE*, and Weiyu Su

***Abstract*—In this article, a hybrid control strategy considering zero-voltage-switching (ZVS) of the inverter within a wide load range is proposed for LCC–LCC compensated electric vehicles wireless charging system. The modified asymmetric voltage cancellation and half-bridge (HB) control modes are combined to satisfy output requirements. Based on the hybrid control strategy, constant-current and constant-voltage outputs can be easily achieved by fixed-frequency phase shift without complex control and additional auxiliary circuits. A time-domain model considering harmonics and rectifier load is developed, based on which an optimal parameter design method is presented for the hybrid control strategy to achieve ZVS and minimize circulating reactive power. Finally, a 3.3 kW experimental prototype is built to verify the feasibility of the proposed method. The results show that ZVS can be achieved over the range of 10–100% rated output power. Compared with the conventional hybrid control strategy that combines symmetric phase shift and HB control, the efficiency can be improved by 1.2–3.6% and the maximum efficiency is 94.1%.**

***Index Terms*—Asymmetric voltage cancellation (AVC), constant current/constant voltage (CC/CV), electric vehicles (EVS), wireless power transfer (WPT), zero-voltage-switching (ZVS).**

NOMENCLATURE

SPS	Symmetric phase shift.
MAVC	Modified asymmetric voltage cancellation.
HB	Half bridge.
S_1–S_4	MOSFETS of the inverter.
D_1–D_4	Diodes of the rectifier.
L_{f1}	Primary compensation inductance.
L_{f2}	Secondary compensation inductance.
L_p	Self-inductance of the transmitter coil.
L_s	Self-inductance of the receiver coil.
C_{f1}	Primary parallel compensation capacitance.
C_{f2}	Secondary parallel compensation capacitance.
C_p	Primary series compensation capacitance.
C_s	Secondary series compensation capacitance.
M	Mutual inductance the magnetic coupler.
k	Coupling coefficient of the magnetic coupler.
U_{dc}	Input dc voltage.
u_{in} (i_{in})	Input voltage (current) of compensation network.
u_o (i_o)	Output voltage (current) of compensation network.
i_p (i_s)	Current of the transmitter (receiver) coil.
α	Phase shift angle of SPS control mode.
β	Phase shift angle of MAVC control mode.
γ	Phase shift angle of HB control mode.
λ	Defined coefficient in MAVC control mode.
U_b (I_b)	Battery charging voltage (current).
U_{bN} (I_{bN})	Nominal battery charging voltage (current).
R_b	Equivalent battery resistance.
R_{bmax}	Maximum equivalent battery resistance.
R_{bmin}	Minimum equivalent battery resistance.
R_{eq}	Equivalent resistive load of the rectifier.
Z_{eq}	Equivalent inductive load of the rectifier.
θ_{eq}	Impedance angle of Z_{eq}.
Z_{in_n}	Input impedance of the nth harmonic.
θ_{in_n}	Input impedance angle of the nth harmonic.
I_{cr}	Critical turn-OFF current of the MOSFET.
C_{ds}	Drain-source capacitance of the MOSFET.
t_d	Dead time of the MOSFET.
$r_{cp,de}$	Rate of decrease of the capacitance C_p.
$r_{cs,in}$	Rate of increase of the capacitance C_s.
P_o	Battery charging power.
P_{in}	Input power of the compensation network.
P_{loss_av}	Average power loss.
η_{av}	Average transfer efficiency.
I_{bs}	Charging current at the moment of control switching.
$t_{off\text{-}on}$	Time from OFF to ON for S_3.
$h_{rcp,de}$ (h_λ)	Iteration step length of $r_{cp,de}$ (λ).

Received 17 June 2024; revised 14 October 2024; accepted 5 December 2024. Date of publication 12 December 2024; date of current version 28 January 2025. This work was supported by the Key Program of the National Natural Science Foundation of China under Grant 51437005. Recommended for publication by Associate Editor C. K. Lee. *(Corresponding author: Bo Zhang.)*

The authors are with the School of Electric Power, South China University of Technology, Guangzhou 510640, China (e-mail: 202220114484@mail.scut.edu.cn; epbzhang@scut.edu.cn; 202220114494@mail.scut.edu.cn).

Color versions of one or more figures in this article are available at https://doi.org/10.1109/TPEL.2024.3516821.

Digital Object Identifier 10.1109/TPEL.2024.3516821

I. INTRODUCTION

COMPARED with traditional conductive power transfer, wireless power transfer (WPT) is considered a promising technology due to its safety, convenience, and flexibility [1], [2], [3]. WPT has been widely used for medical implants [4], [5], smart homes [6], [7], consumer electronics [8], and electric vehicles (EVs) [9], [10], [11], [12]. Specifically, by employing

WPT technology, the charging process of EVs can be achieved automatically with the help of an assisted parking system. As a result, drivers can get rid of manually operating bulky and dangerous cables. With the development of autonomous driving technology, wireless charging will play a crucial role in the EVs market.

Usually, high-performance lithium-ion batteries are used in EVs. According to the typical charging profile of the battery, constant current (CC) and constant voltage (CV) charging modes should be adopted to improve the battery's lifetime and safety [13], [14]. The battery equivalent resistance, which is defined as the ratio of charging voltage to current, gradually increases with charging time. Therefore, accurate regulation of charging current and voltage under variable load is essential. Furthermore, to improve system efficiency, reduce electromagnetic interference (EMI), and suppress voltage spike of MOSFETS, the zero-voltage-switching (ZVS) operation of the inverter is also required [15], [16]. Researchers have proposed several methods to achieve the goals mentioned above, which can be divided into four types.

The first method is to add auxiliary circuits, including dc–dc converter [17], [18], ZVS branch [19], [20], switch-controlled capacitor [21], [22], and dc-controlled variable inductor [23], [24]. In these papers, some circuit components or switches are used to increase the controllable degree of freedom so that the ZVS and the output requirements can be achieved simultaneously, but this method inevitably increases system cost, complexity, and power loss.

The second method is frequency control. In [25] and [26], a self-oscillating control strategy is proposed to achieve CV output and ZVS operation. However, frequency variations over a wide range increase the reactive power and the overall efficiency is poor, especially when the operating frequency is far from the resonant frequency. Therefore, the variable frequency phase shift control strategy is widely adopted to reduce the range of frequency variations. In [15], a three-loop control strategy is proposed based on variable frequency phase shift. Moreover, the author also develops a method for accurate phase detection [27], which enables dynamic adjustment of frequency and phase shift angle to optimize the ZVS angle under various output requirements. However, the coupling between the ZVS angle loop and the voltage/current loop may lead to control instability. In addition to closed-loop control based on phase detection, the frequency can also be obtained by iterative calculation [16] and curve fitting [28]. Although these numerical methods of frequency calculation avoid coupling between control loops, frequency jittering may occur during practical operation.

The third method is active rectification control. Active rectification offers an extra phase shift angle at the secondary rectifier compared to passive rectification. By controlling the respective phase shift angles of the inverter and rectifier, impedance matching of the load can be performed to reduce reactive power and improve efficiency. However, the hard switching would occur easily. Therefore, the third phase shift between the primary and secondary side is introduced as an extra control variable to realize ZVS operation [29]. In [30] and [31], three phase shift angles are jointly optimized to ensure the ZVS of all switches. However, active rectification control requires the primary and secondary phases to be synchronized quickly and accurately, which is difficult due to data delay and signal interference.

The fourth method is to design component parameters [32], [33], [34]. In [32], the effect of each component of LCC–LCC topology on the output current and input impedance angle is investigated, and then the parameters are designed to implement the ZVS, but not the CC/CV outputs. In [33] and [34], the CC and CV outputs are realized at two different frequencies, one of which is much higher than the other, increasing switching loss and EMI.

Furthermore, the full-bridge (FB) and half-bridge (HB) modes of the inverter are usually combined to maintain high efficiency while considering ZVS [28], [35]. In FB mode, the asymmetric voltage cancellation (AVC) control exhibits better performance than the conventional symmetric phase shift (SPS) control for ZVS operation [36]. However, most of the previous studies on AVC have only considered the fundamental harmonic. For some high-order compensation topologies like LCC, where the turn-OFF current of switches contains a large number of high-order harmonics, the fundamental harmonic approximation (FHA) is not accurate enough for ZVS analysis.

In this article, the hybrid control of AVC with HB is investigated considering harmonics and rectifier load based on the LCC–LCC topology. It is found that the ZVS operation of the four switches cannot all be achieved for AVC control under light load, so a modified asymmetric voltage cancellation (MAVC) control strategy is proposed to replace the AVC. Then, through designing optimal component parameters, CC/CV outputs and ZVS over a wide load range can be achieved, and the system maintains high efficiency. The main advantages of the proposed method are as follows.

1) The frequency is fixed at 85 kHz according to the standard in SAE TIR J2954, and only the phase shift control is used to achieve the CC and CV outputs, providing robust control stability.
2) Additional auxiliary circuits are not required for ZVS.
3) The proposed hybrid control of MAVC with HB improves the system efficiency significantly compared to the common hybrid control of SPS with HB.

The rest of this article is organized as follows. Section II develops time-domain models in different control modes of the inverter and gives the ZVS operation conditions. Section III selects optimal parameters to implement the ZVS and discusses the parameter constraints. Then, the ZVS analysis in different control modes is covered in Section IV. Section V validates the proposed strategy with experiments. Finally, Section VI concludes this article.

II. Time-Domain Analysis in Different Control Modes

A. Control Modes of the Inverter

Fig. 1 shows the circuit diagram of the LCC–LCC compensated WPT system, which consists of an inverter powered by a dc source U_{dc}, a compensation network, and a rectifier with batteries. S_1–S_4 and D_1–D_4 are power switches of the inverter and rectifier diodes, respectively. L_{f1}, C_{f1}, and C_{p} are the compensation inductance, parallel compensation

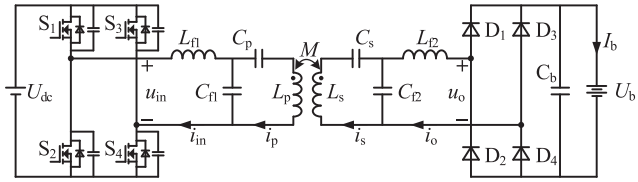

Fig. 1. LCC–LCC compensated WPT topology.

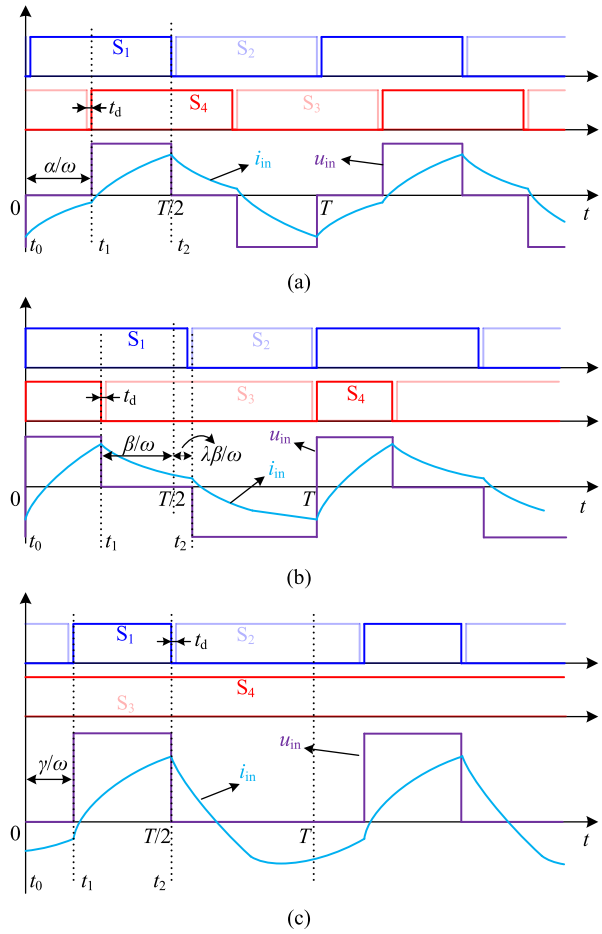

Fig. 2. Typical waveforms for different control mode. (a) SPS mode. (b) MAVC mode. (c) HB mode.

capacitance, and series compensation capacitance of the primary side, respectively. Similarly, L_{f2}, C_{f2}, and C_s are the corresponding parameters of the secondary side. L_p and L_s are self-inductance of transmitter and receiver coils, and M is the mutual inductance. The coupling coefficient k between the coils is defined as $k = M/(L_pL_s)^{1/2}$. The input voltage and current are denoted by u_{in} and i_{in}. The output voltage and current are denoted by u_o and i_o. Moreover, i_p and i_s are currents of transmitter and receiver coils, respectively.

The different control modes of the inverter can be obtained by regulating the switching sequence of the S_1–S_4, as shown in Fig. 2. T and t_d represent the switching period and dead time. In Fig. 2(a), the SPS control enables the inverter to generate a fundamental voltage from 0 to U_m by adjusting the phase shift angle α, where U_m is the maximum fundamental voltage that can be generated by the inverter. However, considering the inverter's ZVS, the combination of AVC and HB has superior performance than the SPS. Fig. 2(b) and (c) display the two control modes, where β and γ are the phase shift angles, and λ is a coefficient defined in this article. It can be noted that AVC control occurs when $\lambda = 0$. However, the ZVS cannot be implemented for all switches when β is closed to π in the AVC control mode. Therefore, this article proposes the MAVC control strategy, as shown in Fig. 2(b). By setting $\lambda > 0$, the ZVS for each of the four switches can be achieved. A detailed analysis will be presented in Section IV.

In order to accurately analyze the ZVS operation conditions, harmonics are not negligible, so it is necessary to establish the time-domain model of the u_{in} under different control modes. Through Fourier series decomposition, u_{in} for different control modes can be derived as

$$u_{in} = \frac{a_0}{2} + \sum_{n=1,2,3,\ldots} \left[\sqrt{a_n^2 + b_n^2} \sin\left(n\omega t + \operatorname{arctg} \frac{a_n}{b_n} \right) \right] \tag{1}$$

where ω is switching angular frequency.

For SPS control mode, a_0, a_n, and b_n are expressed as

$$\begin{cases} a_0 = 0 \\ a_n = -\frac{2U_{dc}}{n\pi} \sin n\alpha \\ b_n = \frac{2U_{dc}}{n\pi} [\cos n\alpha + 1]. \end{cases} \tag{2}$$

For MAVC control mode

$$\begin{cases} a_0 = -\frac{U_{dc}}{\pi}(1-\lambda)\beta \\ a_n = \frac{U_{dc}}{n\pi} [\sin n(\pi + \lambda\beta) + \sin n(\pi - \beta)] \\ b_n = \frac{U_{dc}}{n\pi} [2 - \cos n(\pi + \lambda\beta) - \cos n(\pi - \beta)]. \end{cases} \tag{3}$$

For HB control mode

$$\begin{cases} a_0 = \frac{U_{dc}}{\pi}(\pi - \gamma) \\ a_n = -\frac{U_{dc}}{n\pi} \sin n\gamma \\ b_n = \frac{U_{dc}}{n\pi} [\cos n\gamma - \cos n\pi]. \end{cases} \tag{4}$$

B. Equivalent Impedance of the Rectifier Load

Considering a diode rectifier connected to a resistor under continuous conduction mode (CCM), the equivalent load is typically regarded as a pure resistance $R_{eq} = 8R_b/\pi^2$, where R_b is equivalent battery resistance. However, the equivalent method of pure resistance leads to significant error due to the nonlinear characteristics of the rectifier, especially at light load. Therefore, this section analyzes the rectifier characteristics and establishes a more accurate load model.

It should be noted that the rectifier may operate in the discontinuous conduction mode (DCM) with increasing R_b during the charging process, which would make it extremely difficult to establish a mathematical model. However, DCM can be avoided by reasonable parameter design and some other methods. For example, Li et al. [37] proposed a series LC filter on the L_{f2} branch, which can recover the CCM operation from DCM without changing the original system characteristics. Therefore,

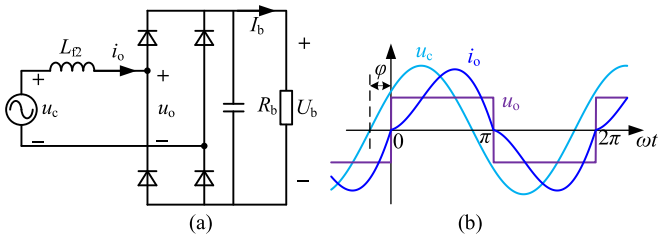

Fig. 3. (a) Simplified secondary equivalent circuit. (b) Voltage and current waveforms under CCM.

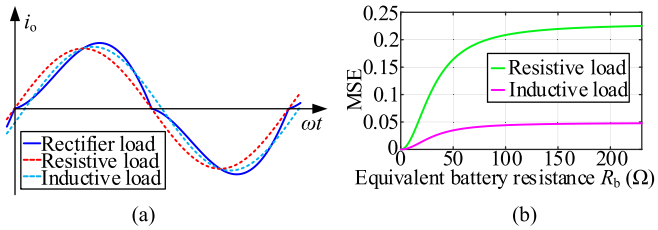

Fig. 4. Comparison between equivalent resistive load and inductive load. (a) Current waveforms when $R_b = 40\ \Omega$ and $U_{cm} = 100$ V. (b) MSE curves.

subsequent analysis of this article is based on the CCM without considering the DCM.

The voltage u_c of capacitor C_{f2} can be replaced by a sinusoidal voltage source because of the negligible current harmonics in coils [37], as shown in Fig. 3(a). The expression of u_c is given as

$$u_c = U_{cm}\sin(\omega t + \varphi) \tag{5}$$

where U_{cm} and φ are the voltage amplitude and initial phase angle of the sinusoidal voltage source.

Fig. 3(b) shows actual voltage and current waveforms. For ease of analysis, i_o is assumed to transform from negative to positive at $t = 0$, and only the positive half period is taken into consideration because of symmetry. Then, the following equation can be developed:

$$U_{cm}\sin(\omega t + \varphi) = L_{f2}\frac{di_o}{dt} + U_b \tag{6}$$

where U_b can also represented by the average value of i_o in the positive half period, as shown in

$$\frac{1}{\pi}\int_0^{\pi} i_o d\omega t = \frac{U_b}{R_b}. \tag{7}$$

If $\omega t = \pi$, It can be obtained that $i_o = 0$. Additionally, combining (6) and (7), the expression for i_o in one period can be derived as

$$i_o(t) = \begin{cases} \frac{U_{cm}}{\omega L_{f2}}\left[-\cos(\omega t+\varphi) - \frac{2\cos\varphi}{\pi}\omega t + \cos\varphi\right], 0 \le t < \frac{\pi}{\omega} \\ \frac{U_{cm}}{\omega L_{f2}}\left[-\cos(\omega t+\varphi) + \frac{2\cos\varphi}{\pi}\omega t - 3\cos\varphi\right], \frac{\pi}{\omega} \le t < \frac{2\pi}{\omega} \end{cases} \tag{8}$$

where $\varphi = \text{arctg}(\omega L_{f2}/R_b)$. It can be seen that i_o contains not only the sinusoidal function but also a linear function, which depends on the L_{f2} and R_b. Analyzing and modeling of the system are quite difficult when dealing with such a nonsinusoidal function, so it is necessary to find a sinusoidal function to replace the actual expression of i_o. Without a doubt, the fundamental component of i_o is a great option. Thus, by applying the Fourier decomposition for (8), the fundamental component i_{o_1} can be obtained as

$$i_{o\_1}(t) = \frac{U_{cm}\sqrt{16(4-\pi^2)\cos^2\varphi + \pi^4}}{\pi^2\omega L_{f2}} \times \sin\left[\omega t + \text{arctg}\frac{(8-\pi^2)R_b}{\pi^2\omega L_{f2}}\right]. \tag{9}$$

TABLE I
PARAMETERS OF THE WPT SYSTEM AT RESONANCE

Parameter	Value	Parameter	Value
U_{dc}	400 V	f_0	85 kHz
k	0.2	M	35 μH
L_p	172.8 μH	L_s	175.5 μH
L_{f1}	30.7 μH	L_{f2}	59.2 μH
C_p	24.2 nF	C_s	30.2 nF
C_{f1}	116.9 nF	C_{f2}	59.4 nF
R_{f1}	35 mΩ	R_{f2}	50 mΩ
R_p	210 mΩ	R_s	212 mΩ
R_b(CC)	15–23 Ω	R_b(CV)	23–230 Ω
I_b(CC)	12 A	I_b(CV)	12–1.2 A

Furthermore, the fundamental component of u_o can also be derived as

$$u_{o\_1}(t) = \frac{8U_{cm}\cos\varphi}{\pi^2}\sin\omega t. \tag{10}$$

Combining (9) and (10), the equivalent impedance Z_{eq} of rectifier load is expressed as follows:

$$Z_{eq} = \frac{8\omega L_{f2}\cos\left(\text{arctg}\frac{\omega L_{f2}}{R_b}\right)}{\sqrt{16(4-\pi^2)\cos^2\left(\text{arctg}\frac{\omega L_{f2}}{R_b}\right) + \pi^4}} e^{j\text{arctg}\frac{(\pi^2-8)R_b}{\pi^2\omega L_{f2}}}. \tag{11}$$

As seen in (11), the rectifier load is inductive rather than resistive if i_o is substituted with i_{o_1}. To compare the inductive load with the conventional resistive load intuitively, the waveforms of i_o under different load models are shown in Fig. 4(a) with the parameters in Table I. The current waveform of the inductive load is clearly more in line with that of the rectifier load. Additionally, mean square error (MSE) is used to quantify the degree of fit, which is defined as

$$\text{MSE} = \frac{1}{\pi}\int_0^{\pi}\left(i_o - \hat{i}_o\right)^2 d\omega t \tag{12}$$

where i_o is the input current of the actual rectifier load; $\hat{i}_o$is the input current of the equivalent resistive or inductive load.

Fig. 4(b) shows the trend of MSE with R_b for the two load models. The MSE of the inductive load is substantially smaller than that of the conventional resistive load, indicating that the

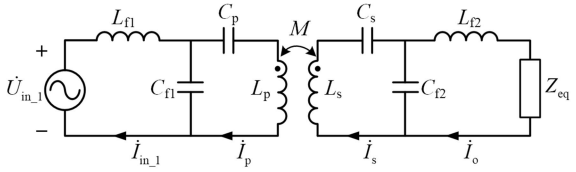

Fig. 5. Fundamental harmonic equivalent circuit of the LCC–LCC topology.

equivalent impedance represented by (11) can more precisely reflect the characteristics of the rectifier load.

C. Derivation of Input Current I_{in} in Different Control Modes

When considering the fundamental harmonic, the output voltage of the inverter can be regarded as a voltage source, and the rectifier load is substituted by (11), as shown in Fig. 5.

According to Kirchhoff's voltage law (KVL) and Kirchhoff's current law (KCL), the system equations based on FHA are expressed as

$$\mathbf{A}\begin{bmatrix}\dot{I}_{\text{in\_1}}\\ \dot{I}_{\text{p}}\\ \dot{I}_{\text{s}}\\ \dot{I}_{\text{o}}\end{bmatrix}=\begin{bmatrix}\dot{U}_{\text{in\_1}}\\ 0\\ 0\\ 0\end{bmatrix} \tag{13}$$

where the matrix **A** is shown in (22), shown at the bottom of the next page. By solving (13), the fundamental input impedance $Z_{\text{in\_1}}$ can be acquired as

$$Z_{\text{in\_1}}=a_{11}+\frac{{a_{12}}^2}{\frac{{a_{23}}^2 a_{44}}{a_{33}a_{44}-{a_{34}}^2}-a_{22}} \tag{14}$$

where a_{ij} denotes the element in row i and column j of the matrix **A**. Additionally, the input impedance angle $\theta_{\text{in\_1}}$ can be expressed as $\theta_{\text{in\_1}}=\text{arctg}(\text{Im}\,Z_{\text{in\_1}}/\text{Re}\,Z_{\text{in\_1}})$.

Specifically, if the component parameters satisfy

$$\begin{cases}\omega L_{\text{f1}}=\frac{1}{\omega C_{\text{f1}}},\omega(L_{\text{p}}-L_{\text{f1}})=\frac{1}{\omega C_{\text{p}}}\\ \omega L_{\text{f2}}=\frac{1}{\omega C_{\text{f2}}},\omega(L_{\text{s}}-L_{\text{f2}})=\frac{1}{\omega C_{\text{s}}}.\end{cases} \tag{15}$$

The current $\dot{I}_{\text{o}}$ is derived as (16) by substituting (15) into (13)

$$\dot{I}_{\text{o}}=\frac{M\dot{U}_{\text{in\_1}}}{\text{j}\omega L_{\text{f1}}L_{\text{f2}}}. \tag{16}$$

It can be seen that the output current is independent of the load at the resonance shown in (15), which is beneficial for CC charging of the battery.

Because L_{f1}, C_{f1}, and L_{p} constitute a low-pass filter, the circuit can be simplified to a branch consisting of L_{f1} and C_{f1} when considering high-order harmonics. Therefore, the input impedance of the nth harmonic is expressed as

$$Z_{\text{in}\_n}=\text{j}\left(n\omega L_{\text{f1}}-\frac{1}{n\omega C_{\text{f1}}}\right),n=2,3,\ldots. \tag{17}$$

For SPS control mode, combining (1), (2), (14), and (17), i_{in} can be calculated as

$$i_{\text{in,SPS}}=\frac{4U_{\text{dc}}\cos\frac{\alpha}{2}}{\pi\left|Z_{\text{in\_1}}\right|}\times\sin\left(\omega t-\frac{\alpha}{2}-\theta_{\text{in\_1}}\right)+\sum_{n=3,5,\ldots}\left[\frac{4U_{\text{dc}}\cos\frac{n\alpha}{2}}{n\pi\left|n\omega L_{\text{f1}}-\frac{1}{n\omega C_{\text{f1}}}\right|}\times\sin\left(n\omega t-\frac{n\alpha+\pi}{2}\right)\right]. \tag{18}$$

For MAVC control mode, combining (1), (3), (14), and (17), i_{in} can be calculated as

$$\begin{aligned}i_{\text{in,MAVC}}=&\frac{\sqrt{2}U_{\text{dc}}\sqrt{3+\cos(1+\lambda)\beta+2(\cos\beta+\cos\lambda\beta)}}{\pi\left|Z_{\text{in\_1}}\right|}\\&\times\sin\left(\omega t+\text{arctg}\frac{a_1}{b_1}-\theta_{\text{in\_1}}\right)\\&+\sum_{n=2,3,\ldots}\left\{\frac{\sqrt{2}U_{\text{dc}}\sqrt{3+\cos n(1+\lambda)\beta-2[\cos n(\pi-\beta)+\cos n(\pi+\lambda\beta)]}}{n\pi\left|n\omega L_{\text{f1}}-\frac{1}{n\omega C_{\text{f1}}}\right|}\right.\\&\left.\times\sin\left(n\omega t+\text{arctg}\frac{a_n}{b_n}-\frac{\pi}{2}\right)\right\}.\end{aligned} \tag{19}$$

For HB control mode, combining (1), (4), (14), and (17), i_{in} can be calculated as

$$\begin{aligned}i_{\text{in,HB}}=&\frac{2U_{\text{dc}}\cos\frac{\gamma}{2}}{\pi\left|Z_{\text{in\_1}}\right|}\times\sin\left(\omega t-\frac{\gamma}{2}-\theta_{\text{in\_1}}\right)\\&+\sum_{n=2,3,\ldots}\left[\frac{\sqrt{2}U_{\text{dc}}\sqrt{1-\cos n\gamma\cos n\pi}}{n\pi\left|n\omega L_{\text{f1}}-\frac{1}{n\omega C_{\text{f1}}}\right|}\right.\\&\left.\times\sin\left(n\omega t+\text{arctg}\frac{a_n}{b_n}-\frac{\pi}{2}\right)\right].\end{aligned} \tag{20}$$

D. Conditions for ZVS Operation

Fig. 2 shows the output voltage and current waveforms of the inverter when ZVS is achieved. Taking SPS control as an example, to realize ZVS for S_4, i_{in} must be kept negative until the moment when S_3 is turned OFF. Then, the drain-source capacitor must be completely discharged within the dead time. To realize ZVS for S_2, i_{in} must be kept positive until the moment when S_1 is turned OFF, and the drain-source capacitor must be completely discharged within the dead time. The ZVS conditions for S_1 and S_3 are identical to those for S_4 and S_2, respectively. It can be seen that the ZVS operation is related to the turn-OFF current, the dead time t_{d} and the drain-source capacitor C_{ds}. Table II summarizes the ZVS operation conditions in different control modes, where I_{cr} is the critical turn-OFF current and can be expressed as [32]

$$I_{\text{cr}}=\frac{2C_{\text{ds}}U_{\text{dc}}}{t_{\text{d}}} \tag{21}$$

TABLE II
OPERATION CONDITIONS FOR ZVS

Control mode	Time	ZVS operation conditions
SPS	$t_1 = \alpha/\omega$	S_3,S_4: $i_{in,SPS}(t_1) < -I_{cr}$
	$t_2 = \pi/\omega$	S_1,S_2: $i_{in,SPS}(t_2) > I_{cr}$
MAVC	$t_0 = 0$	S_1,S_4: $i_{in,MAVC}(t_0) < -I_{cr}$
	$t_1 = (\pi-\beta)/\omega$	S_3: $i_{in,MAVC}(t_1) > I_{cr}$
	$t_2 = (\pi+\lambda\beta)/\omega$	S_2: $i_{in,MAVC}(t_2) > I_{cr}$
HB	$t_1 = \gamma/\omega$	S_1: $i_{in,HB}(t_1) < -I_{cr}$
	$t_2 = \pi/\omega$	S_2: $i_{in,HB}(t_2) > I_{cr}$

III. OPTIMAL PARAMETERS SELECTION AND CONSTRAINTS

A. Selection of the Optimal Parameters

Equation (16) indicates that the LCC–LCC compensation network is suitable for CC charging of the battery due to the load-independent current output characteristics when the parameters are designed in accordance with (15). However, the charging current should be gradually decreased with increasing R_b during CV stage. Without adding extra circuits, the CV output is usually achieved by phase shift control, causing hard switching, and increasing the loss of switches.

To satisfy the ZVS conditions, the system input impedance must be inductive by adjusting frequency or designing component parameters. This article focuses on the latter considering the problems of control instability and EMI caused by frequency variation. The selection of optimal parameters is crucial for ZVS, which has been analyzed in [32]. According to [32], C_p and C_s are selected as the optimal component parameters to implement the ZVS.

To simplify the analysis, parameters of the WPT system at resonance are summarized in Table I. Based on (13) and power conservation, charging current I_b can be calculated as

$$I_b = \frac{8}{\pi^2} |Y_b| U_{dc} \cos\theta_{eq} \tag{23}$$

where θ_{eq} is the impedance angle of (11), and the admittance Y_b is

$$Y_b = \frac{a_{12}a_{23}a_{34}}{(a_{11}a_{22} - a_{12}^2)(a_{34}^2 - a_{33}a_{44}) + a_{11}a_{23}^2a_{44}}. \tag{24}$$

The trend of I_b with R_b for different parameter change ratios can be plotted according to (23), as shown in Fig. 6. As can be seen in Fig. 6(a), I_b is extremely insensitive to the variations of C_p. Fig. 6(b) shows that I_b is slightly influenced in the CC stage by changing C_s, and the maximum fluctuation of the current is less than 3%. In the CV stage, the change of C_s leads to a considerable decrease in I_b and brings I_b closer to the ideal charging current, which is beneficial for ZVS operation.

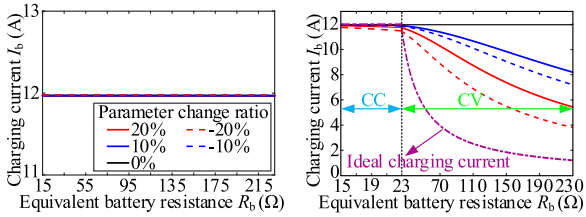

Fig. 6. I_b versus R_b when adjusting component parameters. (a) C_p. (b) C_s.

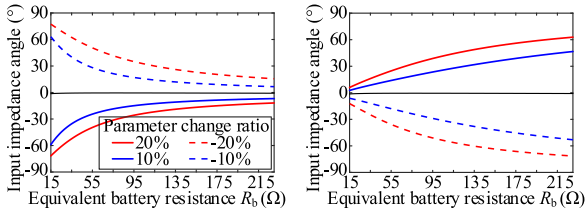

Fig. 7. Input impedance angle versus R_b when adjusting component parameters. (a) C_p. (b) C_s.

Fig. 7 shows the fundamental input impedance angle versus R_b under different parameter change ratios. As C_p decreases or C_s increases, the input impedance becomes more inductive. Therefore, decreasing C_p and increasing C_s are the optimal ways to implement the ZVS.

B. Parameter Constraints for CC Mode

To ensure the charging quality, the influence of parameters on I_b in the CC stage must be considered. Setting I_b in the CC stage satisfies $0.95I_{bN} \le I_b \le I_{bN}$, where I_{bN} is the nominal charging current. Fig. 6 shows that decreasing C_p has a negligible effect on I_b, whereas I_b is decreased when increasing C_s, especially as R_b increases. So, the parameter constraints should be obtained when R_b reaches its maximum in the CC mode (i.e., $R_b = 23\ \Omega$). The three-dimensional view of I_b with the change ratio of C_p and C_s has been plotted in Fig. 8, where $r_{cp,de}$ and $r_{cs,in}$ represent the decrease rate of C_p and increase rate of C_s. The red boundary curve can be obtained by crossing the surface of I_b with the plane of $0.95I_{bN}$ and projecting the intersection line to the $r_{cp,de}$-$r_{cs,in}$ plane. It is obvious that the range of parameter variation is restricted to the left region of the boundary curve.

$$\mathbf{A} = \begin{bmatrix} \mathrm{j}\left(\omega L_{f1} - \frac{1}{\omega C_{f1}}\right) & \mathrm{j}\frac{1}{\omega C_{f1}} & 0 & 0 \\ \mathrm{j}\frac{1}{\omega C_{f1}} & \mathrm{j}\left(\omega L_p - \frac{1}{\omega C_p} - \frac{1}{\omega C_{f1}}\right) & -\mathrm{j}\omega M & 0 \\ 0 & -\mathrm{j}\omega M & \mathrm{j}\left(\omega L_s - \frac{1}{\omega C_s} - \frac{1}{\omega C_{f2}}\right) & \mathrm{j}\frac{1}{\omega C_{f2}} \\ 0 & 0 & \mathrm{j}\frac{1}{\omega C_{f2}} & \mathrm{j}\left(\omega L_{f2} - \frac{1}{\omega C_{f2}}\right) + Z_{eq} \end{bmatrix}. \tag{22}$$

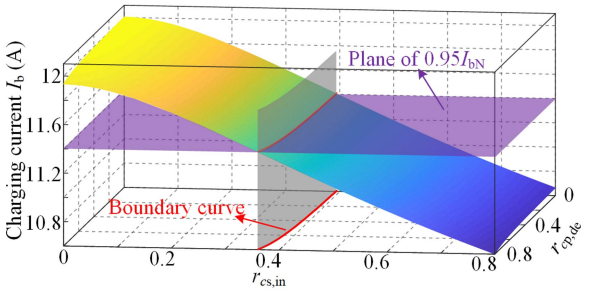

Fig. 8. Three-dimensional view of I_b with the decrease ratio of C_p and the increase ratio of C_s when $R_b = 23\ \Omega$.

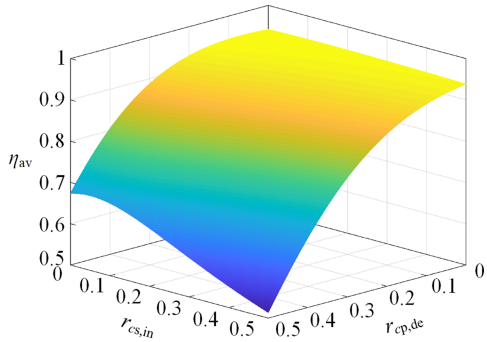

Fig. 9. Average transfer efficiency η_{av} versus $r_{cp,de}$ and $r_{cs,in}$.

IV. ZVS Analysis in Hybrid Control

A. Efficiency Analysis

Minimizing reactive power is one of the most important goals while implementing ZVS, so this section focuses on the transfer efficiency of the system.

According to (13), the current of each branch can be acquired by

$$\begin{cases} \dot{I}_o = Y_b \dot{U}_{in\_1}, \dot{I}_s = Y_1 \dot{U}_{in\_1} \\ \dot{I}_p = Y_2 \dot{U}_{in\_1}, \dot{I}_{in\_1} = Y_3 \dot{U}_{in\_1} \end{cases} \tag{25}$$

where Y_1, Y_2, and Y_3 are expressed as

$$\begin{cases} Y_1 = \frac{a_{34}\left(a_{11}a_{22}-{a_{12}}^2\right)Y_b - a_{12}a_{23}}{a_{11}{a_{23}}^2 + a_{33}\left({a_{12}}^2 - a_{11}a_{22}\right)} \\ Y_2 = \frac{a_{11}a_{23}Y_1 + a_{12}}{{a_{12}}^2 - a_{11}a_{22}}, Y_3 = \frac{1-a_{12}Y_2}{a_{11}}. \end{cases} \tag{26}$$

The fundamental input voltage U_{in_1} in CC mode can be directly expressed by U_{dc} due to the constant-current output characteristic, but in CV mode, U_{in_1} is determined by the load and component parameters because of phase shift control. It can be derived as

$$U_{in\_1} = \begin{cases} \frac{2\sqrt{2}}{\pi} U_{dc}, \text{CC} \\ \frac{\sqrt{2}\pi U_{bN}}{4|Y_b|R_b \cos\theta_{eq}}, \text{CV} \end{cases} \tag{27}$$

where U_{bN} is the nominal charging voltage in the CV stage. Furthermore, it is easy to determine the charging power under the two modes as

$$P_o = \begin{cases} {I_{bN}}^2 R_b, \text{CC} \\ \frac{{U_{bN}}^2}{R_b}, \text{CV}. \end{cases} \tag{28}$$

If the power loss of rectifier is neglected, combining (25), (27), and (28), the transfer efficiency can be obtained as

$$\eta = \begin{cases} \frac{1}{1+\frac{8{U_{dc}}^2}{\pi^2 {I_{bN}}^2 R_b}\left(|Y_b|^2 R_{f2} + |Y_1|^2 R_s + |Y_2|^2 R_p + |Y_3|^2 R_{f1}\right)}, \text{CC} \\ \frac{1}{1+\frac{\pi^2}{8|Y_b|^2 R_b \cos^2\theta_{eq}}\left(|Y_b|^2 R_{f2} + |Y_1|^2 R_s + |Y_2|^2 R_p + |Y_3|^2 R_{f1}\right)}, \text{CV}. \end{cases} \tag{29}$$

From (28) and (29) it can be seen that both output power and transfer efficiency vary with the load R_b. The efficiency of any single load does not appropriately reflect the overall efficiency in the whole load range. Therefore, an average transfer efficiency η_{av} that can represent the overall efficiency is defined as

$$\eta_{av} = \frac{\frac{1}{R_{bmax}-R_{bmin}}\int_{R_{bmin}}^{R_{bmax}} P_o(R_b)dR_b}{\frac{1}{R_{bmax}-R_{bmin}}\int_{R_{bmin}}^{R_{bmax}} P_{in}(R_b)dR_b} = \frac{\int_{R_{bmin}}^{R_{bmax}} P_o(R_b)dR_b}{\int_{R_{bmin}}^{R_{bmax}} \frac{P_o(R_b)}{\eta(R_b)}dR_b} \tag{30}$$

where R_{bmax} and R_{bmin} are the maximum and minimum equivalent battery resistance, P_{in} is the input power of the compensation network. Then, the average power loss P_{loss_av} of the whole load range can be expressed as

$$P_{loss\_av} = \frac{1}{R_{bmax}-R_{bmin}}\left[\frac{\int_{R_{bmin}}^{R_{bmax}} P_o(R_b)dR_b}{\eta_{av}} - \int_{R_{bmin}}^{R_{bmax}} P_o(R_b)dR_b\right]. \tag{31}$$

Equation (31) shows that for a wireless charging system with given output power and load range, the average power loss P_{loss_av} is only determined by η_{av} and inversely proportional to it. As a result, η_{av} can well reflect the average loss of the whole load range and represent the overall efficiency of the system.

Fig. 9 shows the average transfer efficiency η_{av} for different $r_{cp,de}$ and $r_{cs,in}$. The η_{av} decreases as $r_{cp,de}$ or $r_{cs,in}$ increases. This is because the system will gradually move away from the resonance frequency and more circulating reactive power is injected with increasing $r_{cp,de}$ or $r_{cs,in}$. Moreover, it can be seen that $r_{cp,de}$ has a greater effect on the efficiency than $r_{cs,in}$. Therefore, while designing parameters to achieve ZVS, $r_{cp,de}$ and $r_{cs,in}$ should be kept as small as possible, especially the $r_{cp,de}$.

B. ZVS Analysis in SPS Control Mode

In the CV stage, the output voltage of the inverter is regulated by phase shift control as the charging current I_b decreases, causing hard switching. However, the input impedance can be changed by adjusting the parameters C_p and C_s, which provides the potential of achieving ZVS. Therefore, C_p and C_s should be optimized so that ZVS can be achieved over the whole load range while maximizing system efficiency.

For typical SPS control, the input current $i_{in,SPS}$ at a given load can be calculated by (18). Fig. 10 shows the $i_{in,SPS}(t_1)$ and $i_{in,SPS}(t_2)$ with respect to $r_{cp,de}$ and $r_{cs,in}$ when the charging current $I_b = 4$ A. Furthermore, the plane of the critical turn-OFF

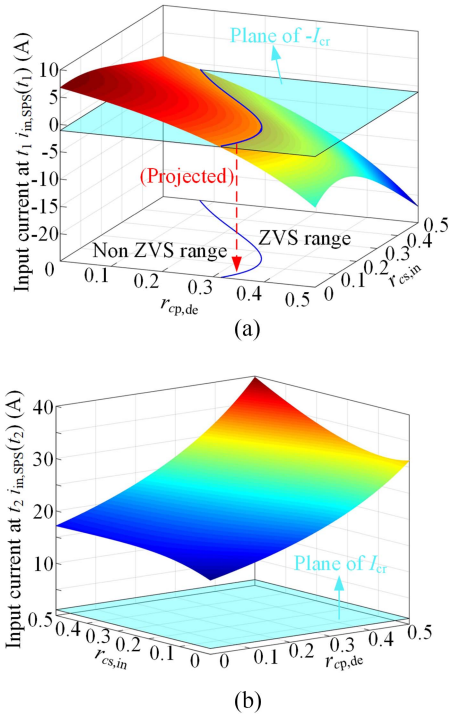

Fig. 10. Input current with respect to $r_{\mathrm{cp,de}}$ and $r_{\mathrm{cs,in}}$ at the moment of (a) t_1 and (b) t_2. (Charging current $I_{\mathrm{b}} = 4$ A in SPS control mode).

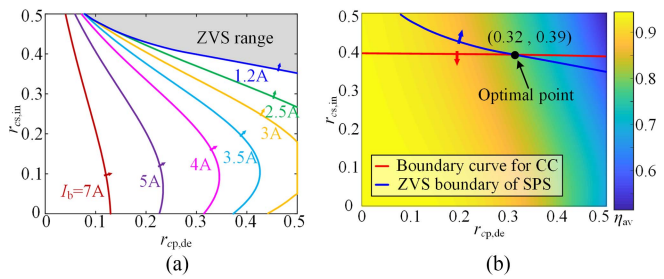

Fig. 11. ZVS situation in SPS control mode. (a) ZVS boundary curves under different I_{b}. (b) ZVS range and η_{av} with respect to $r_{\mathrm{cp,de}}$ and $r_{\mathrm{cs,in}}$.

current I_{cr} is also shown in Fig. 10 ($I_{\mathrm{cr}} = 1.1$ A). According to the ZVS operation conditions in Table II, it can be seen that the ZVS range and non-ZVS range of S_3 and S_4 are divided by the projected bule ZVS boundary curve in Fig. 10(a). S_1 and S_2 can always achieve ZVS over the range of parameters variation, as shown in Fig. 10(b).

Moreover, the ZVS boundary curves for different I_{b} are plotted in Fig. 11(a) to determine the ZVS range over the whole load. The arrows on these curves point to the ZVS range. It can be seen that the ZVS range shrinks as I_{b} decreases, and the final ZVS range will be determined by the minimum charging current of 1.2 A. This is because smaller I_{b} requires a larger phase angle α, resulting in much more challenging to achieve ZVS. Consequently, the values of $r_{\mathrm{cp,de}}$ and $r_{\mathrm{cs,in}}$ will be large to ensure ZVS over a wide load range, which is extremely detrimental to system efficiency.

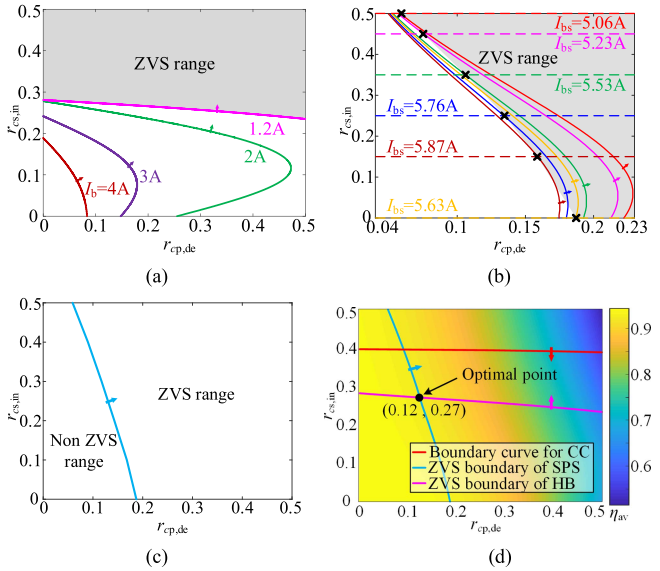

Fig. 12. ZVS situation in SPS+HB control mode. (a) ZVS boundary curves under different I_{b} in HB control mode. (b) ZVS boundary curves under different I_{b} in SPS control mode and curves of I_{bs} under different $r_{\mathrm{cs,in}}$. (c) Fitted ZVS boundary curve in SPS control mode. (d) ZVS range and η_{av} with respect to $r_{\mathrm{cp,de}}$ and $r_{\mathrm{cs,in}}$ in SPS+HB control mode.

Fig. 11(b) displays the ZVS range and average transfer efficiency η_{av} for different $r_{\mathrm{cp,de}}$ and $r_{\mathrm{cs,in}}$ in the SPS control mode. The red curve is the boundary curve of Fig. 8, and the feasible ZVS range is indicated by the arrows of the two curves. In this region, the point with the largest η_{av} is selected as the optimal point of the parameters design. It can be seen that $r_{\mathrm{cp,de}} = 0.32$ and $r_{\mathrm{cs,in}} = 0.39$ at the optimal point, and η_{av} is only 78.84%.

C. ZVS Analysis in SPS+HB Control Mode

When only the SPS control mode is used, the reason for lower efficiency is to satisfy the ZVS requirement under the minimum I_{b}. To improve system efficiency, the hybrid control of SPS and HB is typically used. With the hybrid control mode, the inverter will be switched from SPS to HB mode when I_{b} is small. Fig. 12(a) shows the ZVS boundary curves for various I_{b} in the HB control mode, where the ZVS range is still determined by the minimum I_{b}. However, the ZVS range corresponding to the minimum I_{b} is larger than that in Fig. 11(a), which means that the value of $r_{\mathrm{cp,de}}$ and $r_{\mathrm{cs,in}}$ can be smaller and the system efficiency will be improved. Before applying the hybrid control strategy, it is necessary to calculate the charging current at the moment of control switching, denoted as I_{bs}. Only when the I_{bs} has been calculated can the ZVS in hybrid control mode be precisely analyzed.

From (23), the charging current I_{b} in the CV stage can be expressed as

$$I_{\mathrm{b}} = \frac{2\sqrt{2}}{\pi} |Y_{\mathrm{b}}| \cos\theta_{\mathrm{eq}} U_{\mathrm{in\_1}}. \tag{32}$$

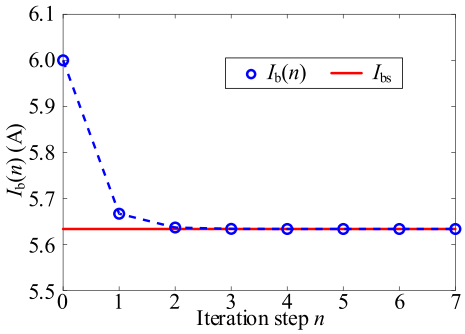

Fig. 13. Iterative values of I_b(n).

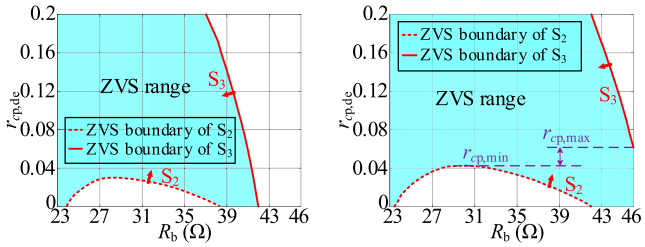

Fig. 14. ZVS range with respect to $r_{cp,de}$ and R_b in MAVC control mode when (a) $r_{cs,in} = 0.3$, $\lambda = 0$ and (b) $r_{cs,in} = 0.3$, $\lambda = 0.15$.

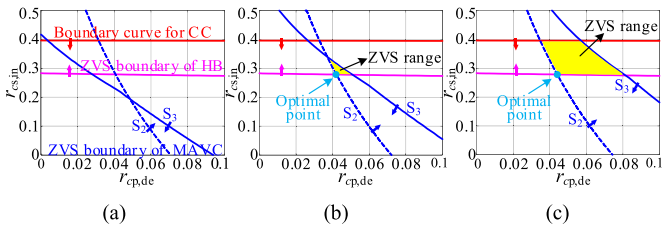

Fig. 15. ZVS range with respect to $r_{cp,de}$ and $r_{cs,in}$ in MAVC+HB control mode when (a) $\lambda = 0.1$, (b) $\lambda = 0.12$, and (c) $\lambda = 0.15$.

U_{in_1} in HB control mode can be derived as follows from (1) and (4):

$$U_{in\_1,HB} = \frac{\sqrt{2}U_{dc}\cos\frac{\gamma}{2}}{\pi} \tag{33}$$

where $\gamma = 0$ at the moment of control switching. Combining (32) and (33) yields

$$I_b = F(I_b) = \frac{4}{\pi^2}|Y_b|\cos\theta_{eq}U_{dc}. \tag{34}$$

By solving (34), the current I_{bs} at the moment of control switching can be obtained. However, such a complicated nonlinear equation cannot be solved analytically. Thus, the numerical solution based on fixed point iteration is applied. The iterative formula is constructed as

$$I_b(n+1) = F\left(I_b(n)\right) \quad n = 0, 1, \ldots \tag{35}$$

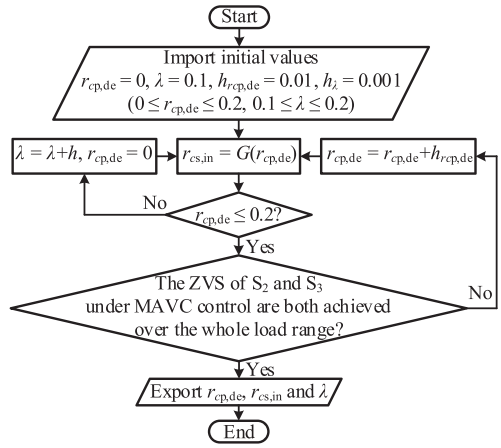

Fig. 16. Flowchart of the parameter calculation.

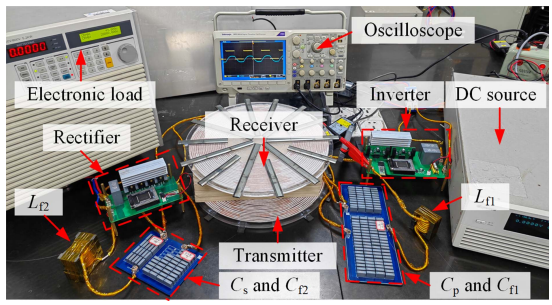

Fig. 17. Experimental prototype.

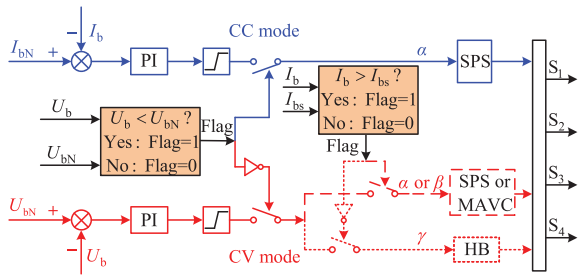

Fig. 18. Control block diagram in different mode.

where taking the initial value of iteration $I_b(0) = I_{bN}/2$. So, I_{bs} can be acquired by

$$I_{bs} = \lim_{n\to\infty} I_b(n). \tag{36}$$

Fig. 13 depicts the relationship between $I_b(n)$ and the iteration step n based on the parameters listed in Table I. It can be seen that $I_b(n)$ quickly converges to I_{bs} as step n increases.

The iteration result is already precise when $n = 4$, so $I_{bs} = I_b(4) = 5.63$ A. It should be noted that I_{bs} must be recalculated when component parameters are changed. As shown in Fig. 6, the variation of the parameter C_p has almost no effect on the charging current I_b, so the value of I_{bs} is only determined by C_s. According to (35) and (36), I_{bs} for different $r_{cs,in}$ can be obtained, as shown by the dashed lines in Fig. 12(b). The

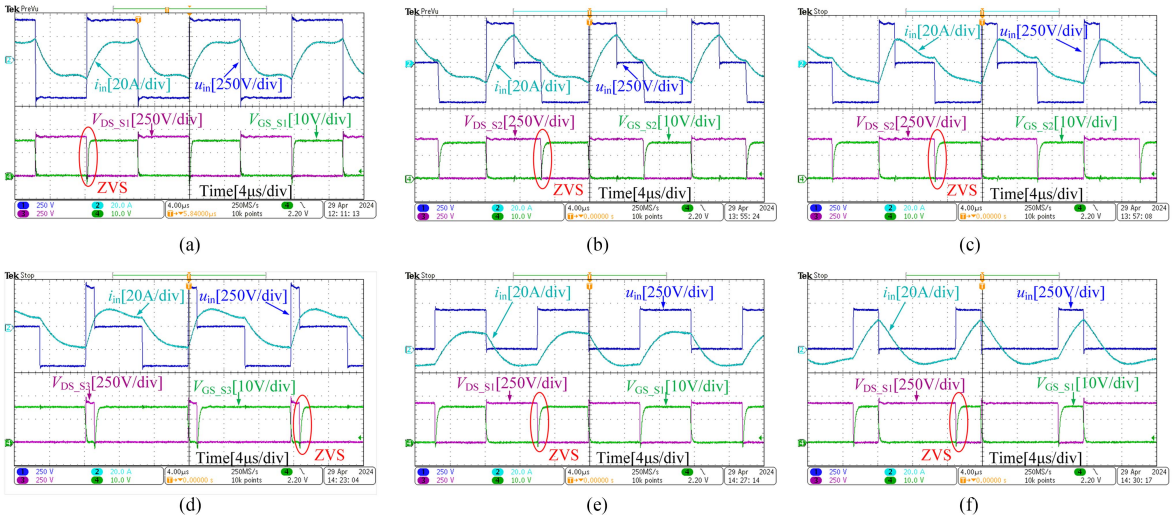

Fig. 19. Steady-state waveforms of the proposed hybrid control of MAVC with HB when (a) $I_b = 12$ A, (b) $I_b = 10$ A, (c) $I_b = 7$ A, (d) $I_b = 5.6$ A, (e) $I_b = 5.5$ A, and (f) $I_b = 3$ A.

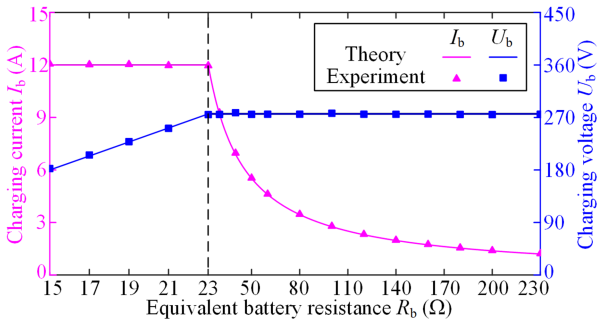

Fig. 20. Charging current and voltage versus the equivalent battery resistance R_b.

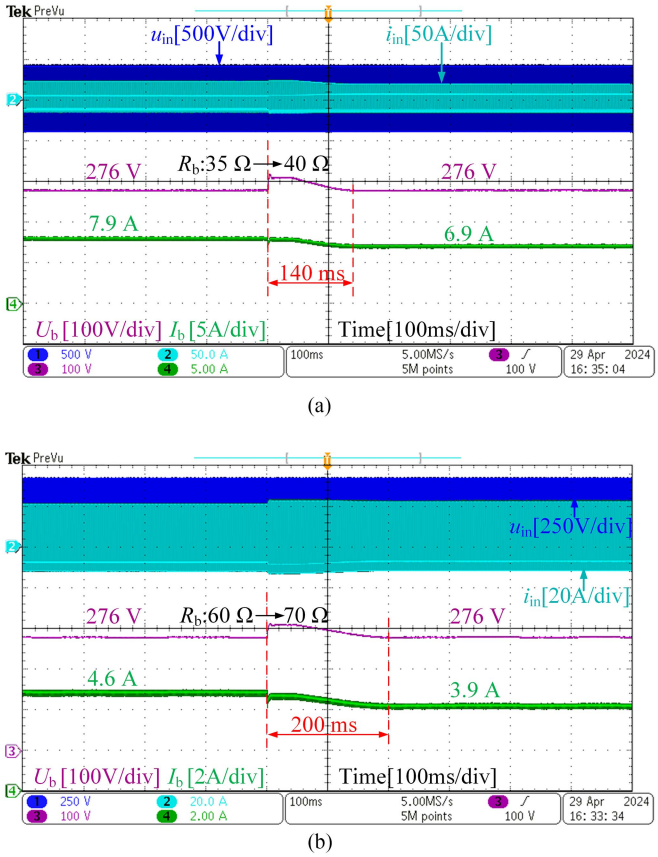

Fig. 21. Dynamic waveforms when the R_b changes (a) from 35 to 40 Ω in the MAVC control mode and (b) from 60 to 70 Ω in the HB control mode.

solid lines represent the ZVS boundary curves under different charging current in the SPS control mode, and the charging current corresponding to these curves are I_{bs} with the same color. Obviously, the ZVS boundary curve of SPS can be fitted by the intersections of curves with same color and the ZVS and non-ZVS range are obtained, as shown in Fig. 12(c).

By combining the ZVS boundary curves of HB and SPS, the ZVS range in the hybrid control mode is obtained, as shown in Fig. 12(d).The baby blue curve represents the ZVS boundary curve in the SPS control mode, and the pink curve represents the ZVS boundary curve in the HB control mode. The common area pointed by the arrows on the three curves is the permitted ZVS range. Compared to SPS control, the combination of SPS and HB control modes broadens the ZVS range. The η_{av} of the optimal point is substantially increased to 92.46%.

D. ZVS Analysis in MAVC+HB Control Mode

The AVC control mode is commonly used instead of the SPS control mode due to its superior ZVS performance. However, ZVS operation of all switches cannot be guaranteed under light load by adopting AVC. It is assumed that $r_{cs,in}$ is 0.3 in order to explain this phenomenon more intuitively. From Fig. 12(a) it can be seen that when $r_{cs,in} = 0.3$, the ZVS condition in the HB control mode can be satisfied regardless of the variation of

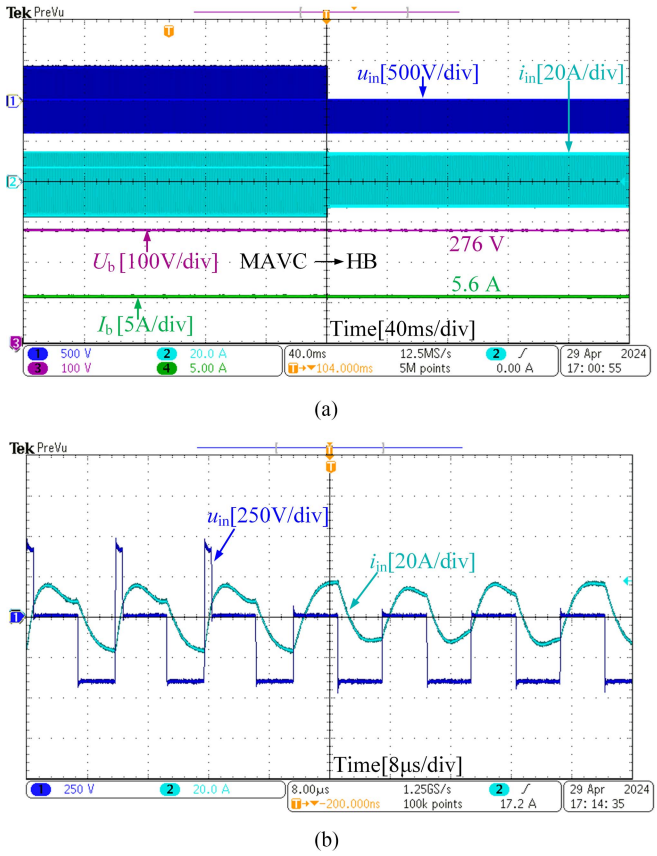

Fig. 22. Dynamic waveforms of control mode switching. (a) Control mode switches from MAVC to HB. (b) Zoom at the moment of switching.

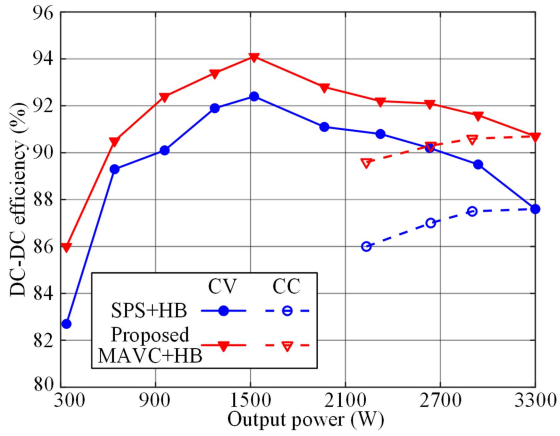

Fig. 23. DC–DC efficiency versus the output power.

$r_{cp,de}$. According to Table II, the ZVS range with $r_{cp,de}$ and R_b in the AVC control mode is shown in Fig. 14(a). The ZVS operation conditions of S_1 and S_4 are always satisfied naturally, so only the ZVS boundary curves of S_2 and S_3 are plotted and indicated by the red dotted and solid lines. It can be seen that the non-ZVS region inevitably exists regardless of $r_{cp,de}$. The main reason is as follows.

As shown in Fig. 2(b), the time $t_{off\text{-}on}$ for S_3 to switch from OFF to ON can be expressed as $t_{off\text{-}on} = (\pi - \beta)/\omega$. If $\lambda = 0$ (i.e., AVC control is employed), the phase shift angle β is quite large and close to π in order to satisfy the requirement of low output power under light load. Therefore, the $t_{off\text{-}on}$ of S_3 is extremely small, which makes it impossible for the current i_{in} to abruptly transition from the negative state of turned OFF to the positive state of turned ON in such a short period of time. As a result, the ZVS of S_3 cannot be achieved under light load. However, if $\lambda > 0$ (i.e., MAVC control is employed), β is smaller for the same output requirement compared to the AVC control, which increases the $t_{off\text{-}on}$ of S_3 and it becomes feasible to realize ZVS even with the light load. Fig. 14(b) shows the ZVS range when $\lambda = 0.15$. When $r_{cp,de}$ is within $[r_{cp,min}, r_{cp,max}]$, the ZVS of all switches can be achieved in the range of full load to half load. So the proposed MAVC should combine with HB to achieve ZVS of a wide range.

Similar to the hybrid control mode of SPS with HB, Fig. 15 shows the ZVS range with $r_{cp,de}$ and $r_{cs,in}$ for different λ in the hybrid control of MAVC with HB. There is no shared ZVS region for the two control modes when $\lambda = 0.1$. As λ increases, the ZVS range begins to form and gradually expands. However, increasing λ causes a larger $r_{cp,de}$ at the optimal point, resulting in lower efficiency. Therefore, there exists an optimal λ such that the optimal point of the parameter design satisfies the ZVS requirements and minimizes the $r_{cp,de}$.

E. Calculation of Optimal Parameters

The previous section shows that multiple variables need to be determined, including $r_{cp,de}$, $r_{cs,in}$, and λ. At the same time, expressions of the ZVS boundary curves cannot be obtained because of the transcendental functions. Consequently, the method of numerical iteration is required to determine the optimal parameters. In order to decrease the computational time and arithmetic requirements on the computer, the ZVS boundary curve of HB is linearly fitted as (37) with the aid of MATLAB

$$r_{cs,in} = G(r_{cp,de}) = -0.086 r_{cp,de} + 0.283, r_{cp,de} \in [0, 0.2]. \tag{37}$$

A flowchart of the optimal parameters calculation for hybrid control of MAVC and HB is shown in Fig. 16. First, a few initial values need to be set, including $r_{cp,de}$, λ, and the corresponding iteration step length $h_{rcp,de}$ and h_λ. Then, $r_{cs,in}$ is calculated according to (37). After that, if the ZVS operation of S_2 and S_3 are both achieved over the whole load range, the parameters are exported and the calculation is finished. Otherwise, $r_{cp,de}$ should be increased based on $h_{rcp,de}$, and $r_{cs,in}$ is recalculated with the new $r_{cp,de}$. The above process is repeated until the ZVS operation conditions is satisfied. Meanwhile, before judging ZVS operation conditions, it is required to determine whether $r_{cp,de}$ is within the limited range. If not, λ should be increased based on h_λ and $r_{cp,de}$ should be reset to the initial value, following which a new iteration computation continues. The calculation process for hybrid control of SPS with HB is similar, which will not be repeated here for space limitation. The results of the calculation are summarized in Table III.

TABLE III
CALCULATION RESULTS OF OPTIMAL PARAMETERS

Hybrid mode	$r_{cp,de}$	$r_{cs,in}$	λ	η_{av}
SPS+HB	0.12	0.27	/	92.46%
Proposed MAVC+HB	0.04	0.28	0.115	93.95%

If ZVS is implemented over the entire load range, the η_{av} is higher in the hybrid control mode of MAVC with HB compared to the SPS with HB hybrid control mode. High transfer efficiency means less reactive circulating current, which will contribute to lower loss of switches and further improve system efficiency. Therefore, the proposed hybrid control of MAVC and HB is chosen as the optimal control strategy.

V. EXPERIMENTAL VERIFICATION

A. Experimental Prototype

To verify the feasibility of the proposed hybrid control strategy, a 3.3 kW experimental prototype is built up, as shown in Fig. 17. The distance between transmitter and receiver coils is 135 mm, and the coupling coefficient $k = 0.2$. Bluetooth communication is used to establish a connection between the primary and secondary sides. An electronic load is employed in replace of the battery, and the equivalent battery resistance R_b varies from 15 Ω to 23 Ω in CC mode and 23 Ω to 230 Ω in CV mode. More detailed parameter information is summarized in Table I, where C_p and C_s are redesigned according to the optimal $r_{cp,de}$ and $r_{cs,in}$ in Table III. As an example, the hybrid control of MAVC and HB results in $C_p = 23.23$ nF and $C_s = 38.66$ nF. The switching current $I_{bs} = 5.6$ A can be calculated by (35) and (36). The inverter consists of four power MOSFETS (IMZA65R027M1H), and the rectifier diodes of the secondary side are IDW40G65C5XKSA1. The controller is a digital signal processor TMS320F28335.

B. CC/CV Operations

Fig. 18 shows the control logic in different control modes. According to the typical two-stage charging profile, the battery should be in CC mode while the charging voltage is less than the nominal voltage U_{bN}, and in CV mode otherwise. Although the constant current output in the CC stage can be achieved by designing parameters reasonably, closed-loop control based on PI is still required considering the fluctuation of the input voltage and component parameters. In the CV stage, the hybrid control strategy is employed. When the charging current I_b exceeds the switching current I_{bs}, the inverter operates in the SPS or MAVC control mode; otherwise, the HB control mode is adopted. The charging voltage can be adjusted and stabilized by controlling the corresponding phase shift angles α, β, and γ under different control modes.

C. Steady-State and Dynamic Performance of the Proposed Hybrid Control of MAVC With HB

Fig. 19 shows the steady-state waveforms of the proposed hybrid control strategy of MAVC with HB under the CV stage. When the charging current $I_b \geq 5.6$ A, the MAVC control is employed; otherwise the HB control is employed, as shown in Fig. 19(a)–(d) and (e)–(f), respectively. It can be observed that with the combination of the two control modes, the ZVS can be realized with a fixed frequency of 85 kHz under various loads. For the CC mode, the constant current output can be realized without closed-loop control because of the reasonable parameters design. Therefore, the steady-state waveforms in CC mode are similar to Fig. 19(a), which is not presented here. The voltage and current variation of the whole charging process is shown in Fig. 20. The experimental results are in excellent agreement with the theoretical charging profile, and the current fluctuation in the CC stage and the voltage fluctuation in the CV stage are both less than 1%.

In order to test the dynamic response of the proposed hybrid control strategy, the load is step-varied under different modes. Fig. 21(a) shows the dynamic waveforms when the resistance R_b suddenly increases from 35 Ω to 40 Ω in the MAVC control mode. The charging voltage U_b can be adjusted to the nominal value of 276 V within 140 ms. Fig. 21(b) shows the dynamic waveforms when the R_b suddenly increases from 60 Ω to 70 Ω in the HB control mode. The U_b is also stabilized at 276 V and the dynamic response time is roughly 200 ms. The dynamic response time is mainly limited by the Bluetooth communication rate, and it can be improved by increasing the baud rate of Bluetooth or using faster Wi-Fi. However, cost and data transfer stability issues must be considered. The detailed study is outside the scope of this article.

The waveforms of the control switching are shown in Fig. 22(a). It is evident that when the control mode changes, the charging current I_b and the charging voltage U_b remain steady, which is beneficial for the battery. Fig. 22(b) shows the enlarged view at the switching moment. The control mode can smoothly switch from MAVC to HB, and the output current of the inverter can be stabilized within a few periods.

D. Efficiency Analysis and Comparison

The measured dc–dc efficiency based on the proposed hybrid control strategy of MAVC with HB under different output power is shown in Fig. 23. In the CC and CV modes, the efficiency range is 89.6–90.7% and 86–94.1%, respectively. For comparison, the efficiency under the hybrid control strategy of SPS with HB is also provided. If the ZVS of four switches is required to achieve over the range of 10–100% nominal output power, the proposed hybrid control strategy of MAVC with HB can improve the system efficiency by 1.2–3.6% compared to the hybrid control strategy of SPS with HB.

Table IV presents the performance comparison with some existing works. Most of the references require additional auxiliary circuits in order to regulate the output voltage and current while implementing ZVS over a wide load range, which inevitably

TABLE IV
COMPARISON WITH EXISTING WORKS

Reference	Rated output power	CC/CV	Coupling coefficient	Frequency	Auxiliary circuit	Output power range of ZVS	Control complexity*	Maximum efficiency
[18]	3.3 kW	CC&CV	0.09–0.21	81.38–90 kHz	Yes	/	Frequency tracking and active rectifier(4)	91.54%
[19]	500 W	No	0.233	85 kHz	Yes	100–500 W	Phase shift(1)	91.7%
[22]	10 W	CC&CV	0.365	85 kHz	Yes	4.6–13.3 W	Switch-controlled capacitor and phase shift(3)	87%
[26]	80 W	CV	0.15–0.39	126.8–141.5 kHz	Yes	30–80 W	Variable frequency(2)	91.5%
[14]	2 kW	CV	0.167	85 kHz	No	0.2–2 kW	Open-loop(1)	92.14%
[15]	500 W	No	0.164–0.22	85–105 kHz	No	/	Variable frequency phase shift(4)	94.19%
[34]	24 W	CC&CV	0.367	206.6/259.9 kHz	No	5–24 W	Frequency switching(1)	93%
This work	**3.3 kW**	**CC&CV**	**0.2**	**85 kHz**	**No**	**0.33–3.3 kW**	**Phase shift(1)**	**94.1%**

*The superscripts (1)–(4) represent the control complexity, i.e., control complexity increases as the number increases.

decreases system efficiency [18], [19], [22], [26]. Additionally, frequency variation of a wide range has also been used to fulfill multiple control objectives but tends to increase the control complexity and lower the stability [15], [26], [34]. However, using the hybrid control strategy and optimal parameter design method proposed in this article, the output requirements of CC/CV and the ZVS of a wide load range can be achieved by fixed-frequency phase shift control only, with a maximum efficiency of 94.1%.

VI. CONCLUSION

This article proposes a hybrid control strategy for the LCC–LCC compensated EVs wireless charging system. Combining the MAVC and HB control modes and designing optimal parameters C_p, C_s, and λ, CC/CV outputs as well as the ZVS with a wide load range can be achieved only by phase shift control. This method eliminates the requirements for auxiliary circuits and complicated control. Meanwhile, in order to analyze the ZVS operation conditions, a time-domain model considering harmonics and the characteristics of the actual rectifier load is developed. Based on the time-domain model, the turn-OFF current of switches can be calculated accurately. A 3.3 kW experimental prototype is built. The results show that the system can implement ZVS over the range of 10–100% nominal output power, and the current fluctuation in the CC stage and the voltage fluctuation in the CV stage are both within 1%. Compared with the conventional hybrid control of SPS and HB, system efficiency can be improved by 1.2–3.6%, with a maximum efficiency of 94.1%.

REFERENCES

[1] G. A. Covic and J. T. Boys, "Modern trends in inductive power transfer for transportation applications," *IEEE J. Emerg. Sel. Topics Power Electron.*, vol. 1, no. 1, pp. 28–41, Mar. 2013.

[2] S. Li and C. C. Mi, "Wireless power transfer for electric vehicle applications," *IEEE J. Emerg. Sel. Topics Power Electron.*, vol. 3, no. 1, pp. 4–17, Mar. 2015.

[3] D. Patil, M. K. McDonough, J. M. Miller, B. Fahimi, and P. T. Balsara, "Wireless power transfer for vehicular applications: Overview and challenges," *IEEE Trans. Transp. Electrific.*, vol. 4, no. 1, pp. 3–37, Mar. 2018.

[4] K. Agarwal, R. Jegadeesan, Y.-X. Guo, and N. V. Thakor, "Wireless power transfer strategies for implantable bioelectronics," *IEEE Rev. Biomed. Eng.*, vol. 10, pp. 136–161, 2017.

[5] L. Li, H. Liu, H. Zhang, and W. Xue, "Efficient wireless power transfer system integrating with metasurface for biological applications," *IEEE Trans. Ind. Electron.*, vol. 65, no. 4, pp. 3230–3239, Apr. 2018.

[6] W. Han, K. T. Chau, and Z. Zhang, "Flexible induction heating using magnetic resonant coupling," *IEEE Trans. Ind. Electron.*, vol. 64, no. 3, pp. 1982–1992, Mar. 2017.

[7] E. Plumed, I. Lope, and J. Acero, "Induction heating adaptation of a different-sized load with matching secondary inductor to achieve uniform heating and enhance vertical displacement," *IEEE Trans. Power Electron.*, vol. 36, no. 6, pp. 6929–6942, Jun. 2021.

[8] S. Y. R. Hui and W. W. C. Ho, "A new generation of universal contactless battery charging platform for portable consumer electronic equipment," *IEEE Trans. Power Electron.*, vol. 20, no. 3, pp. 620–627, May 2005.

[9] U. K. Madawala and D. J. Thrimawithana, "A bidirectional inductive power interface for electric vehicles in V2G systems," *IEEE Trans. Ind. Electron.*, vol. 58, no. 10, pp. 4789–4796, Oct. 2011.

[10] G. Buja, M. Bertoluzzo, and K. N. Mude, "Design and experimentation of WPT charger for electric city car," *IEEE Trans. Ind. Electron.*, vol. 62, no. 12, pp. 7436–7447, Dec. 2015.

[11] W. Li, H. Zhao, J. Deng, S. Li, and C. C. Mi, "Comparison study on SS and double-sided LCC compensation topologies for EV/PHEV wireless chargers," *IEEE Trans. Veh. Technol.*, vol. 65, no. 6, pp. 4429–4439, Jun. 2016.

[12] M. Kim, D.-M. Joo, and B. K. Lee, "Design and control of inductive power transfer system for electric vehicles considering wide variation of output voltage and coupling coefficient," *IEEE Trans. Power Electron.*, vol. 34, no. 2, pp. 1197–1208, Feb. 2019.

[13] K. Song, Z. Li, J. Jiang, and C. Zhu, "Constant current/voltage charging operation for series–series and series–parallel compensated wireless power transfer systems employing primary-side controller," *IEEE Trans. Power Electron.*, vol. 33, no. 9, pp. 8065–8080, Sep. 2018.

[14] Y. Chen et al., "A parameter tuning method for a double-sided compensated IPT system with constant-voltage output and efficiency optimization," *IEEE Trans. Power Electron.*, vol. 38, no. 3, pp. 4124–4139, Mar. 2023.

[15] Y. Jiang, L. Wang, Y. Wang, J. Liu, X. Li, and G. Ning, "Analysis, design, and implementation of accurate ZVS angle control for EV battery charging in wireless high-power transfer," *IEEE Trans. Ind. Electron.*, vol. 66, no. 5, pp. 4075–4085, May 2019.

[16] H. Hu, T. Cai, S. Duan, X. Zhang, J. Niu, and H. Feng, "An optimal variable frequency phase shift control strategy for ZVS operation within wide power range in IPT systems," *IEEE Trans. Power Electron.*, vol. 35, no. 5, pp. 5517–5530, May 2020.

[17] T.-D. Yeo, D. Kwon, S.-T. Khang, and J.-W. Yu, "Design of maximum efficiency tracking control scheme for closed-loop wireless power charging system employing series resonant tank," *IEEE Trans. Power Electron.*, vol. 32, no. 1, pp. 471–478, Jan. 2017.
[18] S. Ann and B. K. Lee, "Analysis of impedance tuning control and synchronous switching technique for a semibridgeless active rectifier in inductive power transfer systems for electric vehicles," *IEEE Trans. Power Electron.*, vol. 36, no. 8, pp. 8786–8798, Aug. 2021.
[19] X. Wang, J. Xu, M. Mao, and H. Ma, "An LCL-based SS compensated WPT converter with wide ZVS range and integrated coil structure," *IEEE Trans. Ind. Electron.*, vol. 68, no. 6, pp. 4882–4893, Jun. 2021.
[20] H. Li, K. Wang, J. Fang, and Y. Tang, "Pulse density modulated ZVS full-bridge converters for wireless power transfer systems," *IEEE Trans. Power Electron.*, vol. 34, no. 1, pp. 369–377, Jan. 2019.
[21] X. Wang, J. Xu, M. Leng, H. Ma, and S. He, "A hybrid control strategy of LCC-S compensated WPT system for wide output voltage and ZVS range with minimized reactive current," *IEEE Trans. Ind. Electron.*, vol. 68, no. 9, pp. 7908–7920, Sep. 2021.
[22] U. D. Kavimandan, S. M. Mahajan, and C. W. Van Neste, "Analysis and demonstration of a dynamic ZVS angle control using a tuning capacitor in a wireless power transfer system," *IEEE J. Emerg. Sel. Topics Power Electron.*, vol. 9, no. 2, pp. 1876–1890, Apr. 2021.
[23] Z. Zhang, F. Zhu, D. Xu, P. T. Krein, and H. Ma, "An integrated inductive power transfer system design with a variable inductor for misalignment tolerance and battery charging applications," *IEEE Trans. Power Electron.*, vol. 35, no. 11, pp. 11544–11556, Nov. 2020.
[24] Z. Zhang et al., "A dynamic wireless power transfer system using DC controlled variable inductor for segment transmitter automatic switching," *IEEE Trans. Power Electron.*, vol. 40, no. 1, pp. 23–27, Jan. 2025.
[25] K. Yan, Q. Chen, J. Hou, X. Ren, and X. Ruan, "Self-oscillating contactless resonant converter with phase detection contactless current transformer," *IEEE Trans. Power Electron.*, vol. 29, no. 8, pp. 4438–4449, Aug. 2014.
[26] L. Xu, Q. Chen, X. Ren, S.-C. Wong, and C. K. Tse, "Self-oscillating resonant converter with contactless power transfer and integrated current sensing transformer," *IEEE Trans. Power Electron.*, vol. 32, no. 6, pp. 4839–4851, Jun. 2017.
[27] Y. Jiang, L. Wang, Y. Wang, J. Liu, M. Wu, and G. Ning, "Analysis, design, and implementation of WPT system for EV's battery charging based on optimal operation frequency range," *IEEE Trans. Power Electron.*, vol. 34, no. 7, pp. 6890–6905, Jul. 2019.
[28] N. Fu, J. Deng, Z. Wang, W. Wang, and S. Wang, "A hybrid mode control strategy for LCC–LCC-compensated WPT system with wide ZVS operation," *IEEE Trans. Power Electron.*, vol. 37, no. 2, pp. 2449–2460, Feb. 2022.
[29] X. Zhang et al., "A control strategy for efficiency optimization and wide ZVS operation range in bidirectional inductive power transfer system," *IEEE Trans. Ind. Electron.*, vol. 66, no. 8, pp. 5958–5969, Aug. 2019.
[30] Y. Jiang, L. Wang, J. Fang, C. Zhao, K. Wang, and Y. Wang, "A joint control with variable ZVS angles for dynamic efficiency optimization in wireless power transfer system," *IEEE Trans. Power Electron.*, vol. 35, no. 10, pp. 11064–11081, Oct. 2020.
[31] Y. Jiang, L. Wang, J. Fang, R. Li, R. Han, and Y. Wang, "A high-efficiency ZVS wireless power transfer system for electric vehicle charging with variable angle phase shift control," *IEEE J. Emerg. Sel. Topics Power Electron.*, vol. 9, no. 2, pp. 2356–2372, Apr. 2021.
[32] F. Wang, W. Zhang, L. Ye, J. Guo, K. Liu, and H. T. Do, "A design method to implement ZVS for electric vehicle wireless charging system with double-side LCC compensation," *IEEE J. Emerg. Sel. Topics Power Electron.*, vol. 9, no. 3, pp. 3791–3801, Jun. 2021.
[33] V.-B. Vu, D.-H. Tran, and W. Choi, "Implementation of the constant current and constant voltage charge of inductive power transfer systems with the double-sided LCC compensation topology for electric vehicle battery charge applications," *IEEE Trans. Power Electron.*, vol. 33, no. 9, pp. 7398–7410, Sep. 2018.
[34] X. Qu, H. Chu, S.-C. Wong, and C. K. Tse, "An IPT battery charger with near unity power factor and load-independent constant output combating design constraints of input voltage and transformer parameters," *IEEE Trans. Power Electron.*, vol. 34, no. 8, pp. 7719–7727, Aug. 2019.
[35] S. Jia, C. Chen, S. Duan, and Z. Chao, "Dual-side asymmetrical voltage-cancelation control for bidirectional inductive power transfer systems," *IEEE Trans. Ind. Electron.*, vol. 68, no. 9, pp. 8061–8071, Sep. 2021.
[36] J. M. Burdio, L. A. Barragan, F. Monterde, D. Navarro, and J. Acero, "Asymmetrical voltage-cancellation control for full-bridge series resonant inverters," *IEEE Trans. Power Electron.*, vol. 19, no. 2, pp. 461–469, Mar. 2004.
[37] W. Li, Q. Zhang, H. Li, C. Cui, and G. Wei, "Series filter computational method for CCM recovery in double side *LCC* WPT system," *IEEE Trans. Ind. Electron.*, vol. 69, no. 9, pp. 8875–8882, Sep. 2022.

Jinlin Peng was born in Sichuan, China, in 1998. He received the B.S. degree in electrical engineering and automation from Fuzhou University, Fuzhou, China, in 2022. He is currently working toward the M.S. degree in power electronics with the School of Electric Power Engineering, South China University of Technology, Guangzhou, China.

His research interest includes wireless power transfer.

Bo Zhang (Fellow, IEEE) was born in Shanghai, China, in 1962. He received the B.S. degree in electrical engineering from Zhejiang University, Hangzhou, China, in 1982, the M.S. degree in power electronics from Southwest Jiaotong University, Chengdu, China, in 1988, and the Ph.D. degree in power electronics from the Nanjing University of Aeronautics and Astronautics, Nanjing, China, in 1994.

He is currently a Professor with the School of Electric Power, South China University of Technology, Guangzhou, China. He has authored or coauthored more than 600 papers and held more than 230 patents. He has authored nine monographs. His research interests include nonlinear analysis and control of power electronics, wireless power transfer technology, and ac drives.

Weiyu Su was born in Shandong, China, in 2000. He received the B.S. degree in electrical engineering and automation in 2022 from South China University of Technology, Guangzhou, China, where he is currently working toward the M.S. degree in power electronics and power drivers.

His current research interest includes wireless power transfer.